

Electromagnetic wave imaging of targets buried in a cluttered medium using a hybrid inversion-DORT method

This article has been downloaded from IOPscience. Please scroll down to see the full text article.

2012 Inverse Problems 28 125008

(<http://iopscience.iop.org/0266-5611/28/12/125008>)

View [the table of contents for this issue](#), or go to the [journal homepage](#) for more

Download details:

IP Address: 194.167.230.229

The article was downloaded on 16/11/2012 at 08:04

Please note that [terms and conditions apply](#).

Electromagnetic wave imaging of targets buried in a cluttered medium using a hybrid inversion-DORT method

Ting Zhang, Patrick C Chaumet¹, Emeric Mudry, Anne Sentenac and Kamal Belkebir

Institut Fresnel (UMR 7249), Aix-Marseille Université, Av. Escadrille Normandie-Niemen, F-13397 Marseille Cedex 20, France

E-mail: patrick.chaumet@fresnel.fr

Received 10 January 2012, in final form 17 October 2012

Published 15 November 2012

Online at stacks.iop.org/IP/28/125008

Abstract

The detection and the characterization of targets buried in a natural medium using an array of monochromatic micro-wave antennas are difficult tasks as medium heterogeneities blur the signature of the objects of interest. In this paper, we propose to couple a nonlinear inversion method to an eigenvector analysis of the time reversal operator (Décomposition de l'Opérateur de Retournement temporel (DORT) technique) for imaging the targets. We show that this combined approach yields much better results than those of the inversion or DORT approaches alone. In particular, it enables us to characterize targets in highly cluttered environments supporting multiple scattering. The efficiency of the technique is illustrated throughout many examples with varying clutter statistics.

(Some figures may appear in colour only in the online journal)

1. Introduction

The detection and the characterization of objects using electromagnetic waves as a probing field are of great interest in many areas, such as non-invasive testing, medical imaging or subsoil probing. In most applications, the imaging issue is made difficult by the inhomogeneities of the natural medium that blur the signature of the targets. Moreover, the emitting and receiving antennas are generally located only on one side of the investigation domain so that the information obtained from the response of the medium to the wave excitation is spatially limited. While numerous mathematical [1] or applied physics [2–4] studies have addressed the problem of target tracking and detection in a noisy environment, a few of them have considered the specific issue of target characterization in a heterogeneous medium.

¹ Author to whom any correspondence should be addressed.

The first issue is to extract the target contribution from the background noisy signature. A tool of choice for this purpose is the time reversal signal technique or its frequency counterpart, the DORT procedure (Décomposition de l'Opérateur de Retournement temporel). The DORT method, originally developed in acoustics [5, 6], was more recently applied to electromagnetic waves [7, 8]. It consists in analysing the eigenvalues and eigenvectors of the time reversal operator (TRO), in order to synthesize incident fields that focus selectively on the targets of interest, thus improving the signal-to-noise ratio. Additional possible data preprocessing such as frequency averaging [9], angular correlation [10] or Wigner–Ville transform [11] can enhance further the target signature. The methods developed for detecting and localizing the targets buried in an inhomogeneous random medium are often based on the manipulation of the TRO [12, 13, 1]. The simplest approach consists in simulating, in a homogeneous average medium, the intensity maps of the dominant eigenvector fields of the TRO and using these maps for pinpointing the targets. These techniques have been shown to be efficient for weakly contrasted clutter where single scattering dominates but have shown their limits in configurations supporting multiple scattering, especially when using only monochromatic data [14–16]. Moreover, they do not provide any useful images for characterizing the targets. For these reasons, inversion techniques which reconstruct the permittivity map of a given investigation domain and which, in their nonlinear versions, can handle configurations supporting multiple scattering [17–21] seem to be an interesting alternative. However, the accuracy of the nonlinear reconstructions is strongly dependent on the signal-to-noise ratio and on the size of the investigation domain [22]. When the targets are buried in an inhomogeneous medium, the investigation domain should be large enough to account properly for the perturbation induced by the clutter. In this case, the inversion requires important computational resources, especially in the three-dimensional vectorial configuration, and often fails because of the large number of unknowns compared to the number of data.

In this paper, we propose to combine the advantages of the nonlinear inversion methods with that of the DORT analysis. We show that this hybrid technique can be used to detect, localize and characterize targets buried in highly contrasted clutter supporting multiple scattering in a much better way than the DORT or classical inversion methods alone. Our analysis is supported by three-dimensional vectorial simulations of an imaging experiment in which two spheres buried in a random inhomogeneous medium are illuminated and observed by an array of monochromatic microwave antennas.

2. Simulation of the imaging experiment and resolution of the forward problem

The three-dimensional imaging configuration simulated in this work is depicted in figure 1. We consider an infinite homogeneous lossless medium of permittivity ε_b . The targets under study are defined by their relative permittivity ε_r and are confined in a domain W . They are surrounded by an inhomogeneous medium with relative permittivity $\varepsilon_c(\mathbf{r}) = \varepsilon_b + \varepsilon_f(\mathbf{r})$, where $\varepsilon_f(\mathbf{r})$ is a random function which is null outside W and whose average is null over W . The entire configuration is non-magnetic. A two-dimensional array of N crossed-dipole monochromatic antennas lying in a plane above W is used to illuminate and observe the scene. This configuration resembles that which is encountered in the detection of buried objects. We have chosen a clutter perturbation with null average in order to dismiss the issue of the interface and to focus on the volume scattering. Note that, in practice this configuration can be obtained with a proper impedance matching of the antennas or an appropriate time windowing. The finite size of the clutter expansion, which is necessary for computation purposes, is chosen wide enough for representing an ‘infinite’ clutter perturbation.

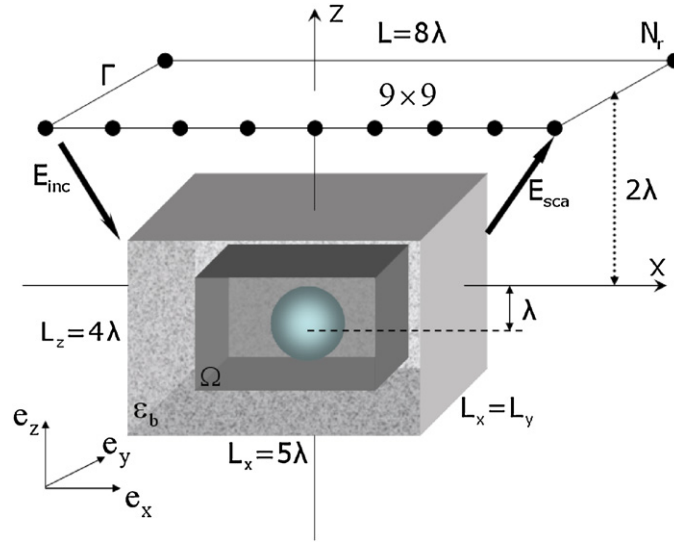


Figure 1. Geometry of the problem. The transmitters and receivers are regularly distributed on a plane, located on one side of the objects. The objects are confined in a disordered medium.

To simulate the data of the imaging experiment, we calculate at the position of the receivers the field scattered by W when the latter is illuminated by an antenna. The forward scattering problem is solved using the coupled dipole method (CDM) that was introduced by Purcell and Pennypacker in 1973 [23]. The CDM method manipulates the local field but in [24] the authors show that the CDM is equivalent to the moments method (MOM) which uses the macroscopic field instead. The self-consistent macroscopic electric field is given by

$$\mathbf{E}_{l,\alpha}(\mathbf{r}) = \mathbf{E}_{l,\alpha}^{\text{inc}}(\mathbf{r}) + \int_W \mathbf{G}(\mathbf{r}, \mathbf{r}') \chi(\mathbf{r}') \mathbf{E}_{l,\alpha}(\mathbf{r}') d\mathbf{r}', \quad (1)$$

and the observation equation is given by

$$\mathbf{E}_{l,\alpha}^{\text{sca}}(\mathbf{r}) = \int_W \mathbf{G}(\mathbf{r}, \mathbf{r}') \chi(\mathbf{r}') \mathbf{E}_{l,\alpha}(\mathbf{r}') d\mathbf{r}', \quad (2)$$

where \mathbf{E} and \mathbf{E}^{sca} denote the total field and the scattered field, respectively. In the following, the position vector \mathbf{r} is written as

$$\mathbf{r} = x\mathbf{e}_x + y\mathbf{e}_y + z\mathbf{e}_z, \quad (3)$$

where \mathbf{e}_x , \mathbf{e}_y and \mathbf{e}_z are unit vectors of a right-handed Cartesian coordinate frame; see figure 1. The orientation of the dipole antenna which generates the electromagnetic incident field that illuminates the scene can take the three orientations, along the x -axis, y -axis, or z -axis. In equations (1) and (2), the subscript l is an integer indexing the dipole and $\alpha = x, y$ or z indicates the direction of the emitting antenna direction. In other words, when $\alpha = x$, \mathbf{E}^{sca} , \mathbf{E} and \mathbf{E}^{inc} correspond to the scattered, total and incident fields that are obtained when the excitation dipole antenna is oriented along the x -axis. The function $\chi(\mathbf{r}')$, whose support is restricted to the scattering domain W , is the linear susceptibility of the object

$$\chi(\mathbf{r}') = \varepsilon(\mathbf{r}') - \varepsilon_b. \quad (4)$$

$\mathbf{G}(\mathbf{r}, \mathbf{r}')$ is the three-dimensional (3D) Green function in the homogeneous infinite medium with permittivity ε_b . Details on the expression and on the numerical computation of 3D Green function can be found in [24, 25].

3. The DORT method

In this section, we recall the properties of the DORT method, especially in the three-dimensional vectorial configuration. We consider an unknown three-dimensional object, made of several scatterers, which is illuminated successively by $l = 1, \dots, N_s$ electromagnetic excitation, figure 1. For each source l , the scattered field is measured at $m = 1, \dots, N_r$ receivers. Assuming that each antenna can play the role of source and receiver, $N_s = N_r = N$. The imaging experiment is summarized into a $N \times N$ symmetric matrix, denoted by \mathbf{K} , such that \mathbf{K}_{ij} represents the scattered field recorded by the j th receiver when the i th antenna is emitting.

In the case of a lossless embedding medium, the time reversal experiment is described by the conjugate transpose matrix \mathbf{K}^\dagger , and the TRO is represented by the self-adjoint matrix $\mathbf{L} = \mathbf{K}^\dagger \mathbf{K}$. In the acoustic case, it has been shown that each significant eigenvalue of the TRO is associated with a single point-like scatterer [6]. In electromagnetism, localizing a scatterer can be achieved by the backpropagation of the corresponding eigenvector, which synthesizes a wave focusing on the scatterer [7, 8].

In the three-dimensional vectorial configuration, one can build the matrix \mathbf{K} under the three orthogonal linear polarizations in order to gain more information. More precisely, for each α -direction of the polarization of the sources, three scattered field components ($\beta = x, y, z$) are measured. Then a (3×3) matrix \mathbf{K}_{ij} can be written as

$$\mathbf{K}_{ij} = \begin{bmatrix} K_{ij}^{xx} & K_{ij}^{xy} & K_{ij}^{xz} \\ K_{ij}^{yx} & K_{ij}^{yy} & K_{ij}^{yz} \\ K_{ij}^{zx} & K_{ij}^{zy} & K_{ij}^{zz} \end{bmatrix}. \quad (5)$$

Diagonal elements of the matrix \mathbf{K}_{ij} describe the relation between receivers and emitters with the same orientation. The off-diagonal elements describe the cross-polarizations. $\mathbf{K}_{ij} = \mathbf{K}_{ij}^T$ due to reciprocity. Thus the $3N \times 3N$ matrix \mathbf{K} is assembled from all the matrix \mathbf{K}_{ij} :

$$\mathbf{K} = \begin{bmatrix} \mathbf{K}_{11} & \mathbf{K}_{12} & \cdots & \mathbf{K}_{1N} \\ \mathbf{K}_{21} & \mathbf{K}_{22} & \cdots & \mathbf{K}_{2N} \\ \vdots & \vdots & \ddots & \vdots \\ \mathbf{K}_{N1} & \mathbf{K}_{N2} & \cdots & \mathbf{K}_{NN} \end{bmatrix}. \quad (6)$$

By virtue of the reciprocity theorem, the matrix \mathbf{K} is symmetric and the TRO is defined as $\mathbf{L} = \mathbf{K}^\dagger \mathbf{K}$. Since \mathbf{L} is a self-adjoint matrix, one can determine the eigenvalues and eigenvectors

$$\mathbf{L}\mathbf{V} = \zeta \mathbf{V}, \quad (7)$$

where the eigenvalue ζ is real and the eigenvectors \mathbf{V} are in the form of

$$\mathbf{V} = [V_{1,x}, V_{1,y}, V_{1,z}, \dots, V_{N,x}, V_{N,y}, V_{N,z}]. \quad (8)$$

Each component of the eigenvector associated with the highest eigenvalue ζ provides the complex amplitudes of the emitting dipoles (former receivers) such that they synthesize an incident field focusing on the brightest scatterer:

$$\mathbf{E}_\zeta^{\text{inc;DORT}}(\mathbf{r}) = \sum_{l=1}^N \sum_{\alpha}^{x,y,z} V_{l,\alpha}(\zeta) \mathbf{E}_{l,\alpha}^{\text{inc}}(\mathbf{r}). \quad (9)$$

The corresponding scattered field is now obtained with the same linear combination as one of the incident fields (equation (9)):

$$\mathbf{E}_\zeta^{\text{sca;DORT}}(\mathbf{r}) = \sum_{l=1}^N \sum_{\alpha}^{x,y,z} V_{l,\alpha}(\zeta) \mathbf{E}_{l,\alpha}^{\text{sca}}(\mathbf{r}). \quad (10)$$

When considering the three-dimensional vectorial limited aspect imaging configuration, one can show that each point-scatterer is associated with three dominant eigenvalues of the operator \mathbf{L} [26].

Hence, in this case, the DORT method provides a means for focusing selectively onto each target with three different incident fields.

4. Inverse scattering problem

The inverse scattering problem is stated as finding the relative permittivity distribution ε_r inside a bounded investigating (or test) domain Ω included into W so that the associated scattered field to a known incident field matches the measured scattered field $\mathbf{f}_{l,\alpha}$. Many iterative methods have been developed for solving such problems. Starting from an initial estimate, one can adjust the parameters of interest by minimizing the cost function involved with the measured scattered field and the incident field. The literature mainly shows two approaches. The first one is the linearized method, including the Newton–Kantorovich method [27] and the distorted-wave Born approach [28, 29]. The total field in the investigated domain is considered fixed at each iteration step, and is the solution of the forward scattering problem equation (1) for the best available estimation of the relative permittivity. The second approach is the nonlinearized method, namely the modified gradient method [30, 31] and the contrast source inversion method [32–34], which consist in updating simultaneously the permittivity as well as the total field inside the test domain Ω . A hybrid method combining ideas from linearized and nonlinearized methods is given in [35]. The reconstruction of several targets with different shapes and constitutive materials using experimental data was presented. It was shown that the best result was obtained with the hybrid method. Hence, we use this method to characterize qualitatively (shape and relative permittivity) the targets present in a cluttered environment.

4.1. Principles of the algorithm

In this hybrid method [36], two sequences related to the contrast and total field inside the test domain, χ_n and $\mathbf{E}_{l,\alpha,n}$, respectively, are built up according to the following recursive relations:

$$\mathbf{E}_{l,\alpha,n} = \mathbf{E}_{l,\alpha,n-1} + \kappa_{l,\alpha,n;\mathbf{v}} \mathbf{v}_{l,\alpha,n} + \kappa_{l,\alpha,n;\boldsymbol{\omega}} \boldsymbol{\omega}_{l,\alpha,n}, \quad (11)$$

$$\chi_n = \chi_{n-1} + \beta_n d_n, \quad (12)$$

where $\mathbf{v}_{l,\alpha,n}$, $\boldsymbol{\omega}_{l,\alpha,n}$ and d_n are updating directions with respect to the total field $\mathbf{E}_{l,\alpha,n}$ and the contrast χ_n , respectively, and $\kappa_{l,\alpha,n}$, β_n are scalar coefficients. The updating directions $\mathbf{v}_{l,\alpha,n}$ and d_n are chosen as the standard Polak–Ribière conjugate-gradient directions [37], while $\boldsymbol{\omega}_{l,\alpha,n}$ is given by

$$\boldsymbol{\omega}_{l,\alpha,n} = \tilde{\mathbf{E}}_{l,\alpha,n-1} - \mathbf{E}_{l,\alpha,n-1} \quad \text{with} \quad \tilde{\mathbf{E}}_{l,\alpha,n-1} = [\mathbf{I} - \mathbf{G}_\Omega \chi_{n-1}]^{-1} \mathbf{E}_{l,\alpha}^{\text{inc}}, \quad (13)$$

where $\tilde{\mathbf{E}}_{l,\alpha,n-1}$ represents the total field inside the test domain Ω , calculated from the coupling equation with contrast χ_{n-1} . Indeed, the scalar weight $\kappa_{l,\alpha,n}$ and β_n are chosen at each iteration step n so as to minimize the normalized cost functional $\mathcal{F}(\chi_n, \mathbf{E}_{l,\alpha,n})$ given by

$$\mathcal{F}_n(\chi_n, \mathbf{E}_{l,\alpha,n}) = W_\Omega \sum_{l=1}^N \sum_{\alpha}^{x,y,z} \|\mathbf{h}_{l,\alpha,n}^{(1)}\|_\Omega^2 + W_\Gamma \sum_{l=1}^N \sum_{\alpha}^{x,y,z} \|\mathbf{h}_{l,\alpha,n}^{(2)}\|_\Gamma^2, \quad (14)$$

where the normalizing coefficients W_Ω and W_Γ are defined as

$$W_\Omega = \frac{1}{\sum_{l=1}^N \sum_{\alpha}^{x,y,z} \|\mathbf{E}_{l,\alpha}^{\text{inc}}\|_\Omega^2}, \quad W_\Gamma = \frac{1}{\sum_{l=1}^N \sum_{\alpha}^{x,y,z} \|\mathbf{f}_{l,\alpha}\|_\Gamma^2}. \quad (15)$$

The subscripts Ω and Γ are included in the norm $\|\cdot\|$ and later in the inner product $\langle \cdot, \cdot \rangle$ to indicate the domain of integration. The functions $\mathbf{h}_{l,\alpha,n}^{(1)}$ and $\mathbf{h}_{l,\alpha,n}^{(2)}$ are two residual errors. The first one is the residual error with respect to the incident field in the test domain computed from the self-consistent function. The second residual error is the error on the scattered field computed from the observation equation

$$\mathbf{h}_{l,\alpha,n}^{(1)} = -\mathbf{E}_{l,\alpha,n} + \mathbf{E}_{l,\alpha}^{\text{inc}} + \mathbf{G}_{\Omega}\chi_n\mathbf{E}_{l,\alpha,n} \quad \text{and} \quad \mathbf{h}_{l,\alpha,n}^{(2)} = \mathbf{f}_{l,\alpha} - \mathbf{G}_{\Gamma}\chi_n\mathbf{E}_{l,\alpha,n}. \quad (16)$$

To ameliorate the inversion procedure, we have used the *a priori* information that both the real and imaginary parts of the sought relative complex permittivity are real and non-negative. Instead of retrieving a complex function χ_n , two real auxiliary functions ξ_n and η_n are reconstructed such that

$$\chi_n = 1 + \xi_n^2 + j\eta_n^2 - \varepsilon_b. \quad (17)$$

The recursive relation with respect to contrast χ_n (equation (12)) becomes

$$\xi_n = \xi_{n-1} + \beta_{n;\xi}d_{n;\xi} \quad \text{and} \quad \eta_n = \eta_{n-1} + \beta_{n;\eta}d_{n;\eta}. \quad (18)$$

As updating directions $d_{n;\xi}$ and $d_{n;\eta}$, the authors take

$$d_{n;\xi} = g_{n;\xi} + \gamma_{n;\xi}d_{n-1;\xi}, \quad \gamma_{n;\xi} = \frac{\langle g_{n;\xi}, g_{n;\xi} - g_{n-1;\xi} \rangle_{\Omega}}{\|g_{n-1;\xi}\|_{\Omega}^2}, \quad (19)$$

$$d_{n;\eta} = g_{n;\eta} + \gamma_{n;\eta}d_{n-1;\eta}, \quad \gamma_{n;\eta} = \frac{\langle g_{n;\eta}, g_{n;\eta} - g_{n-1;\eta} \rangle_{\Omega}}{\|g_{n-1;\eta}\|_{\Omega}^2}, \quad (20)$$

where g_{ξ} and g_{η} are the gradients of the cost functional $\mathcal{F}(\xi, \eta, \mathbf{E}_{l,\alpha,n})$ with respect to ξ and η , respectively, evaluated at the $(n-1)$ th step, assuming that the total field inside the test domain does not change. These gradients are given by

$$g_{n;\xi} = 2\xi_{n-1}\text{Re} \left[W_{\Omega} \sum_{l=1}^N \sum_{\alpha}^{x,y,z} \bar{\mathbf{E}}_{l,\alpha,n-1} \mathbf{G}_{\Omega}^{\dagger} \mathbf{h}_{l,\alpha,n-1}^{(1)} - W_{\Gamma} \sum_{l=1}^N \sum_{\alpha}^{x,y,z} \bar{\mathbf{E}}_{l,\alpha,n-1} \mathbf{G}_{\Gamma}^{\dagger} \mathbf{h}_{l,\alpha,n-1}^{(2)} \right], \quad (21)$$

$$g_{n;\eta} = 2\eta_{n-1}\text{Im} \left[W_{\Omega} \sum_{l=1}^N \sum_{\alpha}^{x,y,z} \bar{\mathbf{E}}_{l,\alpha,n-1} \mathbf{G}_{\Omega}^{\dagger} \mathbf{h}_{l,\alpha,n-1}^{(1)} - W_{\Gamma} \sum_{l=1}^N \sum_{\alpha}^{x,y,z} \bar{\mathbf{E}}_{l,\alpha,n-1} \mathbf{G}_{\Gamma}^{\dagger} \mathbf{h}_{l,\alpha,n-1}^{(2)} \right], \quad (22)$$

where the overbar denotes the complex conjugate, and $\mathbf{G}_{\Omega}^{\dagger}$ and $\mathbf{G}_{\Gamma}^{\dagger}$ are the adjoint operators of \mathbf{G}_{Ω} and \mathbf{G}_{Γ} , respectively. The search direction $\mathbf{v}_{l,\alpha,n}$ for the total field inside the test domain is similar to those chosen for the contrast functions ξ and η :

$$\mathbf{v}_{l,\alpha,n} = \mathbf{g}_{l,\alpha,n;\mathbf{E}_{l,\alpha}} + \gamma_{l,\alpha,n;\mathbf{E}_{l,\alpha}} \mathbf{v}_{l,\alpha,n-1}, \quad (23)$$

$$\gamma_{l,\alpha,n;\mathbf{E}_{l,\alpha}} = \frac{\langle \mathbf{g}_{l,\alpha,n;\mathbf{E}_{l,\alpha}}, \mathbf{g}_{l,\alpha,n;\mathbf{E}_{l,\alpha}} - \mathbf{g}_{l,\alpha,n-1;\mathbf{E}_{l,\alpha}} \rangle_{\Omega}}{\|\mathbf{g}_{l,\alpha,n-1;\mathbf{E}_{l,\alpha}}\|_{\Omega}^2}, \quad (24)$$

where $\mathbf{g}_{l,\alpha,n;\mathbf{E}_{l,\alpha}}$ is the gradient of the cost functional $\mathcal{F}(\xi, \eta, \mathbf{E}_{l,\alpha,n})$ with respect to the field $\mathbf{E}_{l,\alpha}$, evaluated at the $(n-1)$ th step, assuming that ξ and η does not change:

$$\mathbf{g}_{l,\alpha,n;\mathbf{E}_{l,\alpha}} = W_{\Omega} [\mathbf{h}_{l,\alpha,n-1}^{(1)} - \bar{\chi}_{n-1} \mathbf{G}_{\Omega}^{\dagger} \mathbf{h}_{l,\alpha,n-1}^{(1)}] - W_{\Gamma} \bar{\chi}_{n-1} \mathbf{G}_{\Gamma}^{\dagger} \mathbf{h}_{l,\alpha,n-1}^{(2)}. \quad (25)$$

As initial estimate for ξ_0 and η_0 , we use the backpropagation method provided by [38]. Note that, in all the results presented in this work, we have simplified further the reconstruction procedure by assuming that the sought permittivity was real and non-negative. In other words, all the inversions were performed by setting η to zero.

4.2. Derivation of the hybrid inversion-DORT method

It has been shown that the DORT method provides a means for generating incident fields focusing onto a given scatterer. We propose here to introduce this information in the inversion procedure. This idea was first presented in [36] in the simplified 2D scalar configuration and yielded a marked improvement of the targets reconstruction. The main difference between the scalar and vectorial configuration, apart from the increased computational complexity, is that the DORT analysis provides three eigenvectors focusing on each target in the 3D vectorial case, whereas it provides only one eigenvector in the scalar case. Hence, we expect the hybrid inversion-DORT approach to be even more interesting in the 3D vectorial configuration than in the scalar configuration.

To introduce the DORT fields in the inversion procedure, we note $\mathbf{E}_\zeta^{\text{inc:DORT}}$, $\zeta = 1, \dots, N_{\text{ev}}$, the DORT incident fields that focus onto the targets. Here, N_{ev} is the number of the eigenvalues associated with the targets. In our configuration, it is equal, in the absence of noise, to three times the number of targets. The scattered field $\mathbf{f}_\zeta^{\text{DORT}}$ associated with the incident field $\mathbf{E}_\zeta^{\text{inc:DORT}}$ is easily calculated through equation (9) and reads

$$\mathbf{f}_\zeta^{\text{DORT}}(\mathbf{r}) = \sum_{l=1}^N \sum_{\alpha}^{x,y,z} V_{l,\alpha}(\zeta) \mathbf{f}_{l,\alpha}(\mathbf{r}). \quad (26)$$

As described in subsection 4.1, the authors suggest here to use N_{ev} incident field $\mathbf{E}_\zeta^{\text{inc:DORT}}$ and N scattered field $\mathbf{f}_\zeta^{\text{DORT}}$ derived from DORT in the iterative scheme, instead of the incident field $\mathbf{E}_{l,\alpha}^{\text{inc}}$ and the scattered field $\mathbf{f}_{l,\alpha}$. Therefore, the contrast and the total fields in the test domain Ω are determined iteratively by minimizing a cost functional of the form

$$\mathcal{F}_n^{\text{DORT}}(\chi_n, \mathbf{E}_{\zeta,n}^{\text{DORT}}) = W_\Omega^{\text{DORT}} \sum_{\zeta=1}^{N_{\text{ev}}} \|\mathbf{h}_{\zeta,n}^{(1;\text{DORT})}\|_\Omega^2 + W_\Gamma^{\text{DORT}} \sum_{\zeta=1}^{N_{\text{ev}}} \|\mathbf{h}_{\zeta,n}^{(2;\text{DORT})}\|_\Gamma^2, \quad (27)$$

where the residual errors $\mathbf{h}_{\zeta,n}^{(1;\text{DORT})}$ and $\mathbf{h}_{\zeta,n}^{(2;\text{DORT})}$ and the normalizing coefficients W_Ω^{DORT} and W_Γ^{DORT} are similar to those defined previously in equations (15) and (16) but in using the DORT field.

Using the DORT incident fields in the cost functional instead of the fields generated by each antenna (multiplied by the three possible orientations) permits to reduce significantly the number of unknowns of the inverse problem. Indeed, in the latter case, the cost function \mathcal{F}_n is a nonlinear expression with respect to $6N$ complex unknown ($\kappa_{l,\alpha,n;\nu}$, $\kappa_{l,\alpha,n;\omega}$) and two real unknown ($\beta_{n;\xi}$, $\beta_{n;\eta}$), while in the former case the cost function $\mathcal{F}_n^{\text{DORT}}$ depends only on $2N_{\text{ev}}$ complex unknown ($\kappa_{\zeta,n;\nu}$, $\kappa_{\zeta,n;\omega}$) and two real unknown ($\beta_{n;\xi}$, $\beta_{n;\eta}$). Hence, it is expected to reduce drastically the computation time with this procedure.

We now turn to the numerical demonstration of the interest of the inversion-DORT method. Note that, in all the inversion procedures, the size of the investigating domain Ω is smaller than that of the scattering domain W so that the theoretical ingredients that are employed to synthesize and invert the data are different. Both the forward and inverse methods use a mesh size of $\lambda/10$.

5. Numerical study of the performances of the hybrid inversion-DORT method

In this section, we first compare, on a given configuration, the performances of the hybrid inversion-DORT method to that of the DORT or inversion methods alone. Then, we study the robustness of the inversion-DORT technique with respect to the structural noise surrounding the scatterers. Lastly, we point out the interest of using a nonlinear inversion scheme and the full polarized data for retrieving the targets.

5.1. Parameters of the imaging configuration

In most cases, the scattering domain W of the imaging configuration depicted in figure 1 is a box with size $(5\lambda \times 5\lambda \times 4\lambda) \text{ m}^3$, centred at $(0, 0, -\lambda)$ where λ is the illumination wavelength in the homogeneous lossless medium. The radar array is described by a lattice of $N = 81$ antennas regularly distributed on a square of side of 8λ , which is located at $z = 2\lambda$, i.e. λ above the cluttered environment.

The scattering domain includes two dielectric spheres embedded in a highly cluttered environment. The smallest sphere, centred at the origin, has a radius of $\lambda/6$, with relative permittivity $\varepsilon = 3\varepsilon_b$. The largest sphere is located at $(0.5\lambda, 0, -0.7\lambda)$ and has a radius of $\lambda/4$ with the same relative permittivity.

The random permittivity of the clutter, $\varepsilon_f(\mathbf{r})$, is defined as a Gaussian variable with zero mean and standard deviation h and Gaussian correlation function $C(\mathbf{r})$ with correlation length l_c . The Gaussian correlation function C is defined as

$$C(\mathbf{r}) = h^2 \exp\left(-\frac{\|\mathbf{r}\|^2}{l_c^2}\right). \quad (28)$$

In addition to these statistical parameters, we introduce the realization-dependent standard variation $\sigma(\varepsilon_f)$, obtained through a volume averaging over W , to characterize specifically the clutter strength of the given realization.

To quantify more precisely the influence of the clutter, two errors are defined,

$$\text{Err}_s = \frac{\sum_{l=1}^N \sum_{\alpha}^{x,y,z} \|\mathbf{f}_{l,\alpha} - \mathbf{f}_{l,\alpha}^{\text{scatterers}}\|_{\Gamma}^2}{\sum_{l=1}^N \sum_{\alpha}^{x,y,z} \|\mathbf{f}_{l,\alpha}^{\text{scatterers}}\|_{\Gamma}^2}, \quad (29)$$

$$\text{Err}_d = \frac{\sum_{l=1}^N \sum_{\alpha}^{x,y,z} \|\mathbf{f}_{l,\alpha} - \mathbf{f}_{l,\alpha}^{\text{scatterers}} - \mathbf{f}_{l,\alpha}^{\text{clutter}}\|_{\Gamma}^2}{\sum_{l=1}^N \sum_{\alpha}^{x,y,z} \|\mathbf{f}_{l,\alpha}^{\text{scatterers}}\|_{\Gamma}^2}, \quad (30)$$

where $\mathbf{f}_{l,\alpha}$ and $\mathbf{f}_{l,\alpha}^{\text{scatterers}}$ denote the field scattered by the targets with or without the clutter, respectively, and $\mathbf{f}_{l,\alpha}^{\text{clutter}}$ denotes the field scattered by the clutter alone. Err_s is used to quantify the noise level, and Err_d indicates the amount of multiple scattering between the targets and the clutter. If Err_d is small, the targets and the clutter can be considered to radiate independently. Note that for the same statistical parameters, the errors Err_s and Err_d may vary significantly as they depend on the specific realization of the random process.

To quantify the quality of the image, we also define a contrast reconstruction error as

$$\text{Err}_{\chi} = \frac{\|\chi_{\text{actual}} - \chi_{\text{rec}}\|_{\Omega}^2}{\|\chi_{\text{actual}}\|_{\Omega}^2}, \quad (31)$$

where χ_{actual} is the permittivity contrast of the actual objects, while χ_{rec} is the reconstructed permittivity contrast.

Lastly, to indicate the presence of multiple scattering within W , we introduce Err_{born} as

$$\text{Err}_{\text{born}} = \frac{\sum_{l=1}^N \sum_{\alpha}^{x,y,z} \|\mathbf{f}_{l,\alpha} - \mathbf{f}_{l,\alpha}^{\text{born}}\|_{\Gamma}^2}{\sum_{l=1}^N \sum_{\alpha}^{x,y,z} \|\mathbf{f}_{l,\alpha}\|_{\Gamma}^2}, \quad (32)$$

where $\mathbf{f}_{l,\alpha}^{\text{born}}$ is the scattered field computed under the single approximation, i.e. the total field inside the clutter and the targets is assumed to be equal to the incident field.

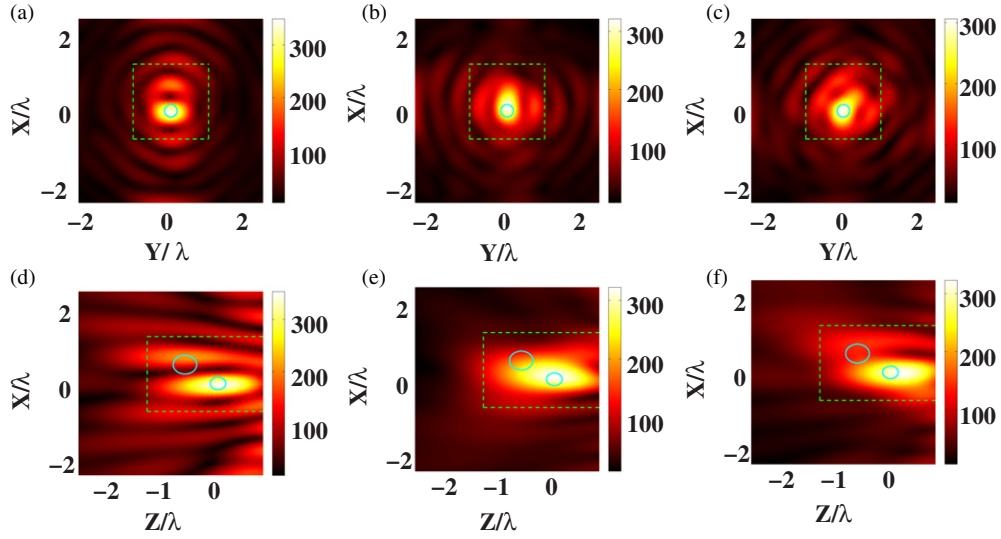


Figure 2. Intensity map in W of the electric field formed by the three eigenvectors of the TRO related to the three largest eigenvalues. These three eigenvectors focus on the sphere which is the closest to the antennas. The clutter is described by $l_c = \lambda/10$, $\sigma(\varepsilon_f) = 0.068\varepsilon_b$ with $\text{Err}_s = 174\%$, $\text{Err}_d = 2\%$ and $\text{Err}_{\text{born}} = 48\%$. (a)–(c) Maps in the (x, y) plane at $z = 0$. (d)–(f) Maps in the (x, z) plane at $y = 0$. Each column corresponds to the first, second and third eigenvalues. The dash box indicates the investigating domain Ω used in the inversion procedure.

5.2. Comparison of the hybrid inversion-DORT method with the DORT and inversion techniques. Influence of the size of the clutter and of its specific permittivity distribution

In this first study, we consider that an uncorrelated clutter (the correlation length $l_c = \lambda/10$ being equal to the mesh size) with a realization-dependent standard deviation of ε_f is $\sigma(\varepsilon_f) = 0.068\varepsilon_b$, yielding $\text{Err}_s = 174\%$, $\text{Err}_d = 2\%$ and $\text{Err}_{\text{born}} = 48\%$, respectively. The values of Err_{born} and Err_d indicate that the configuration supports moderate multiple scattering (within the targets and within the clutter) but that the interaction between the targets and clutter is weak.

We first perform the DORT analysis of the scattered field data. Figures 2 and 3 show the intensity of the electric field radiated by the antennas in the homogeneous medium with permittivity ε_b , with the currents given by the eigenvectors of the TRO. As expected, the first three eigenvalues correspond to the scatterer whose signature on the antennas is dominant. In our configuration, it corresponds to the smallest sphere which is closer to the antennas than the largest one. The fourth to the sixth eigenvalues correspond to the second most important signature, which is that of the largest sphere. There are three eigenvalues focusing on each scatterer, depending on the polarization of the antennas. We have checked that if only one component of polarization is used in the scattered field data, there is only one eigenvalue related to the scatterer, in agreement with the conclusion of [7]. In this incomplete imaging configuration, it is seen that the DORT eigenvectors allow the localization of the two scatterers with a rather large imprecision along the z -axis.

In a second step, we apply the hybrid inversion-DORT method to the scattered field data in order to reconstruct quantitatively the permittivity map of the investigation domain. The investigation domain Ω is limited to the ‘brightest’ region given by the DORT field intensity map, namely a box placed at $[-0.75\lambda, 1.25\lambda] \times [-\lambda, \lambda] \times [-1.5\lambda, \lambda]$, which is indicated by

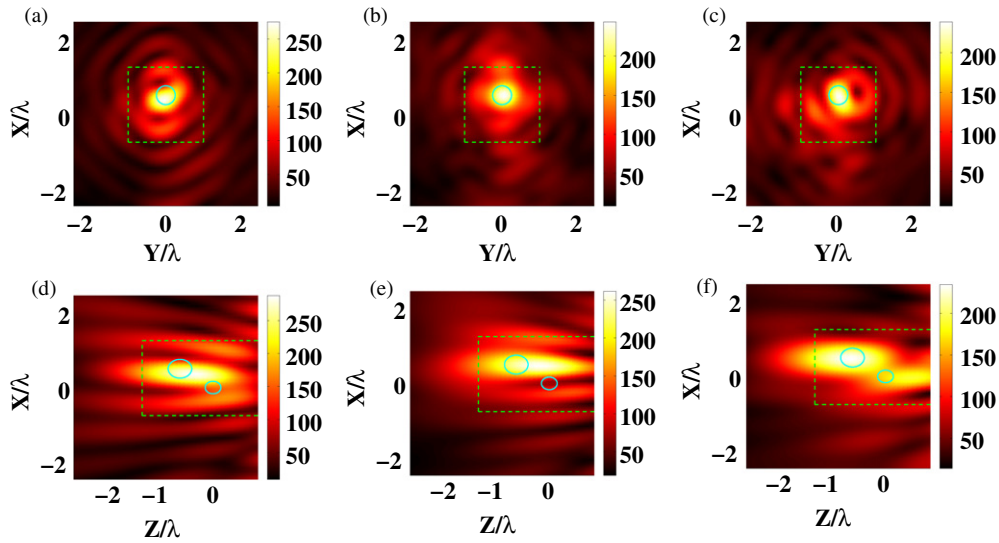


Figure 3. The same as figure 2, but the eigenvectors correspond to the fourth, fifth and sixth eigenvalues. They focus on the sphere which is the furthest from the antennas. (a)–(c) Maps in the (x, y) plane at $z = 0.7\lambda$. (d)–(f) Maps in the (x, z) plane at $y = 0$. Each column corresponds to the fourth, fifth and sixth eigenvalues.

the dashed squares plotted in figures 2 and 3. The inversion procedure is stopped when their cost functions reach a plateau.

Then, we compare the inversion-DORT reconstruction to that obtained with the classical inversion scheme without optimized incident fields, figure 5.

We observe that the inversion-DORT procedure gives a better localization than the DORT method (especially in the z direction) and a better characterization than the classical inversion method alone. The inversion-DORT procedure permits to avoid the ghosts that are present around the targets in the classical reconstruction. This qualitative superiority of the inversion-DORT method is confirmed by the contrast error criterion Err_χ which is equal to 63% for the inversion-DORT and to 153% for the classical inversion. Moreover, the cost function converges more quickly with the hybrid method than with the classical one, the converged value being one order of magnitude, lower in the former case than in the latter. The inversion-DORT computation time, (206 s), is about 200 times shorter than that of the classical inversion scheme. This discrepancy is explained by the number of unknowns and the convergence rate, see figure 5. Indeed, the inversion-DORT method uses only 6 incidences (which correspond to the significant eigenvectors of the TRO), whereas the classical inversion scheme uses 81×3 different incidences which yield 40 times more unknowns.

The inversion-DORT technique can also be used to reconstruct the targets sequentially. In figure 6, we have restricted the investigation domain to a smaller domain Ω_1 (Ω_2) that surrounds the first (second) target. In this case, solely the incident fields focusing on the chosen target are kept in the inversion process. We observe in figure 4 that this sequential reconstruction yields a better estimation of the targets while diminishing the computation time. Of course, with the classical inversion method using non-optimized incident fields the selective reconstruction on Ω_1 and Ω_2 is worse than that obtained with the initial larger investigation domain Ω (not shown).

The size of the scattering domain chosen for these simulations may be thought of too small to mimic accurately a realistic experiment where the targets are buried in an infinite

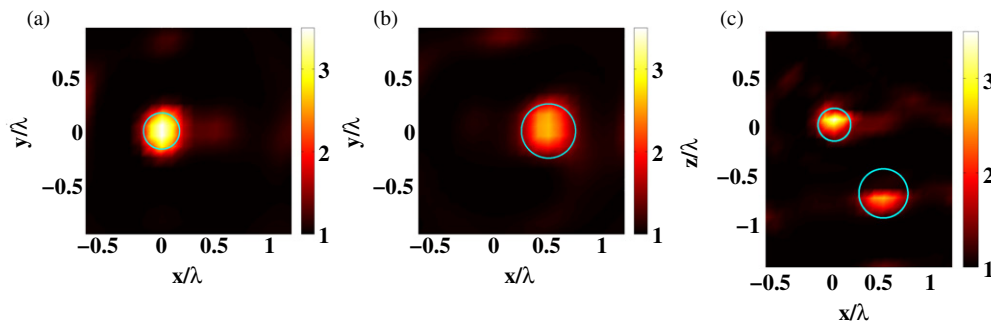


Figure 4. Inversion-DORT reconstructed permittivity obtained for the same configuration as that described in figure 2. (a), (b) Maps in the (x, y) plane at $z = 0$ and $z = -0.7\lambda$, respectively. (c) Map in the (x, z) plane for $y = 0$.

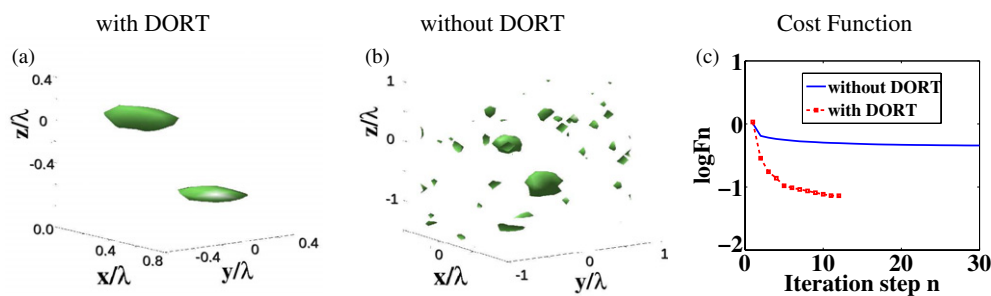


Figure 5. The configuration is the same as that described in figure 2. (a) Iso-surface of the reconstructed permittivity profile at $\varepsilon = 2$ using the inversion-DORT procedure; (b) the same as (a) using the classical inversion procedure; (c) evolution of the cost function (log-scale representation) versus the iteration step using the inversion-DORT method (dashed curve) and classical inversion (solid curve). All these plots correspond to the reconstruction shown in figure 4.

inhomogeneous soil. Indeed, as it stands, the width of W is smaller than the antennas lattice width. We have thus performed other experiments with twice bigger scattering domains to check that the reconstructions provided by the hybrid DORT-inversion procedure were not changed. More precisely, we considered a scattering domain W of size $(10\lambda \times 10\lambda \times 10\lambda)$ that is enlarged by a factor of 2 in the x, y directions and of 2.5 in the z direction as compared to the one chosen in the previous simulation. For a meaningful comparison, we kept exactly the same clutter around the objects as that used in figure 4.

We observe in figure 7 that the six dominant eigenvectors of the TRO for the large scattering domain W yield intensity maps that are very similar to that obtained for the small W , see figures 2 and 3. Hence, even though the noise level ratio Err_s is changed from 171% (small W) to 541% (large W), the DORT analysis still enables us to generate incident fields that focus on the targets.

Then, we see, by comparing figures 4–8, that the reconstruction obtained with the inversion-DORT procedure for large W is very close to that obtained with small W , with similar contrast errors, $\text{Err}_\chi = 68\%$ and 62% , respectively.

This result is not surprising as, with the DORT focusing fields, solely the inhomogeneities close to the targets participate in the scattered field data that are used in the inversion procedure. Note that this property may also be considered a drawback, as it confers an increased

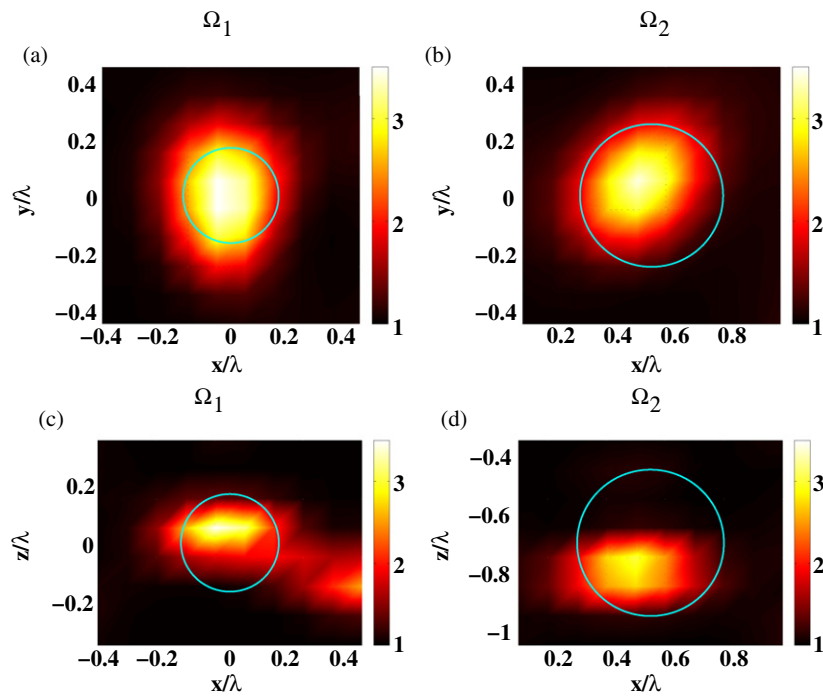


Figure 6. Inversion-DORT reconstructions for the same configuration as that of figure 4, but with investigation boxes that are restricted, successively, to domains surrounding each target, Ω_1 and Ω_2 . Ω_1 is centred at the origin with size $\lambda \times \lambda \times 0.8\lambda$, while Ω_2 is centred at $(0.5\lambda, 0, -0.7\lambda)$ with the same size. (a) Map in the (x, y) plane at $z = 0$ in Ω_1 , (b) map in the (x, y) plane at $z = -0.7\lambda$ in Ω_2 ; (c) map in the (x, z) plane at $y = 0$ in Ω_1 , (d) map in the (x, z) plane at $y = 0$ in Ω_2 .

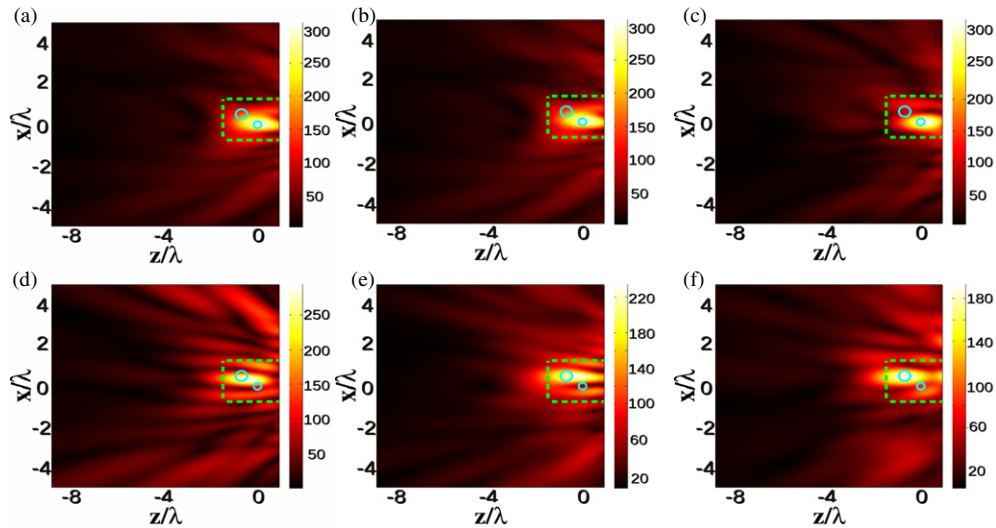


Figure 7. Intensity map of the electric field formed by the eigenvectors of the TRO related to the six largest eigenvalues in the (x, z) plane for $y = 0$ for a configuration similar to that used for figures 2 and 3 except that the scattering domain W is ten times larger.

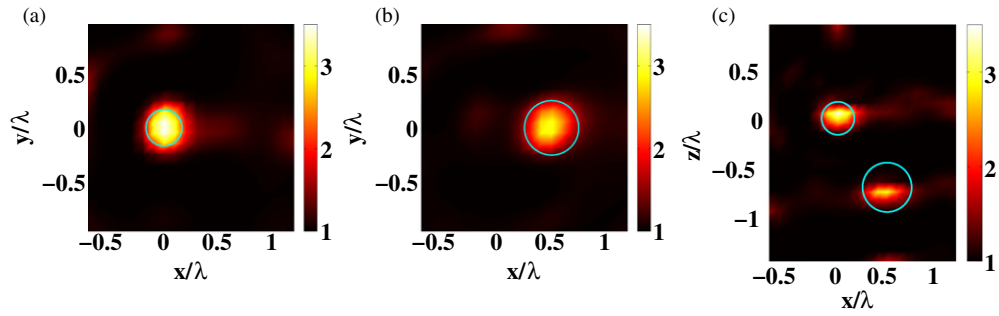


Figure 8. Inversion-DORT reconstructed permittivity for a configuration similar to that used in figure 4 except that the scattering domain W is ten times larger (the investigation domain Ω is kept the same). (a), (b) Maps in the (x, y) plane at $z = 0$ and $z = -0.7\lambda$, respectively. (c) Map in the (x, z) plane at $y = 0$.

importance to the specific clutter distribution surrounding the targets. Thus, to check the generality of our results, we have also verified that the reconstructions obtained for different clutter realizations with the same statistics, were similar [4].

The analysis presented in this section was repeated for different clutter types and always led to the same conclusion: the inversion-DORT is always superior to the classical inversion scheme without optimized incident fields for characterizing the targets and for limiting the computational cost and it ameliorates significantly the information brought by the DORT approach alone, in particular for localizing the target along the z -axis. Moreover, thanks to the studies conducted on large scattering domain and many clutter realizations, we believe that our simulations give a good estimate of the imaging achievements of the inversion-DORT method for realistic geometries in which the targets are buried in an infinite clutter with given statistics. We now describe more precisely the performances of the inversion-DORT method for different clutter types.

5.3. Robustness of the inversion-DORT method with respect to the clutter statistics

In this section, we apply the inversion-DORT method to data stemming from targets buried in different clutter types. We study the robustness of the reconstructions versus increasing clutter standard deviation $\sigma(\varepsilon_f)$, and versus the clutter correlation length l_c .

5.3.1. Influence of the clutter standard deviation. In this section, the correlation length is kept fixed at $l_c = \lambda/10$, while the standard deviation is increased. In the first example, the realization-dependent standard deviation of ε_f , $\sigma(\varepsilon_f) = 0.096\varepsilon_b$, yields $\text{Err}_s \approx 400\%$ and $\text{Err}_d = 2\%$. We observe in figure 9 that the two scatterers are still well localized.

In the second example, the standard deviation reaches $\sigma(\varepsilon_f) = 0.125\varepsilon_b$, leading to $\text{Err}_s = 682\%$ and $\text{Err}_d = 2\%$. In this case, there are only two eigenvectors that focus on the deepest scatterer (the least echogeneous one), as shown in figure 10 but the selective reconstruction of the targets provided by the inversion-DORT method is still satisfactory, see figure 11. Note that, in this case, the reconstruction of the least echogeneous target has been obtained using the only two focusing incident DORT fields.

If the noise is further amplified to reach $\sigma(\varepsilon_f) = 0.145\varepsilon_b$, corresponding to $\text{Err}_s = 900\%$ and $\text{Err}_d = 2\%$, the DORT method does not provide any eigenvectors focusing on the deepest scatterer and the reconstruction is impossible.

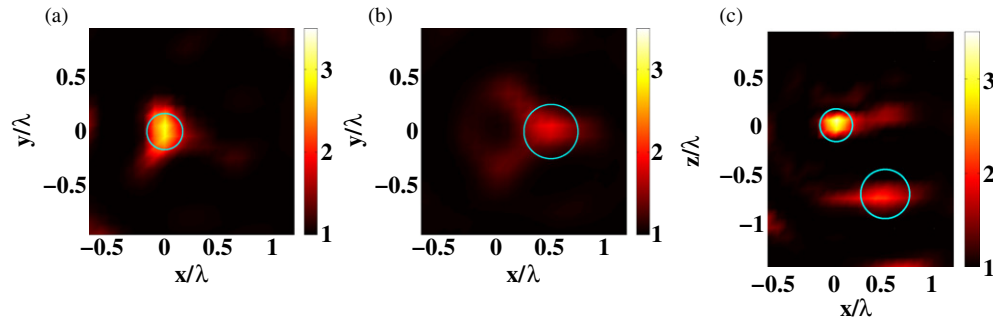


Figure 9. The same as figure 4 but the clutter is defined by $l_c = \lambda/10$, $\sigma(\varepsilon_f) = 0.096\varepsilon_b$ yielding $\text{Err}_s = 400\%$ and $\text{Err}_d = 2\%$.

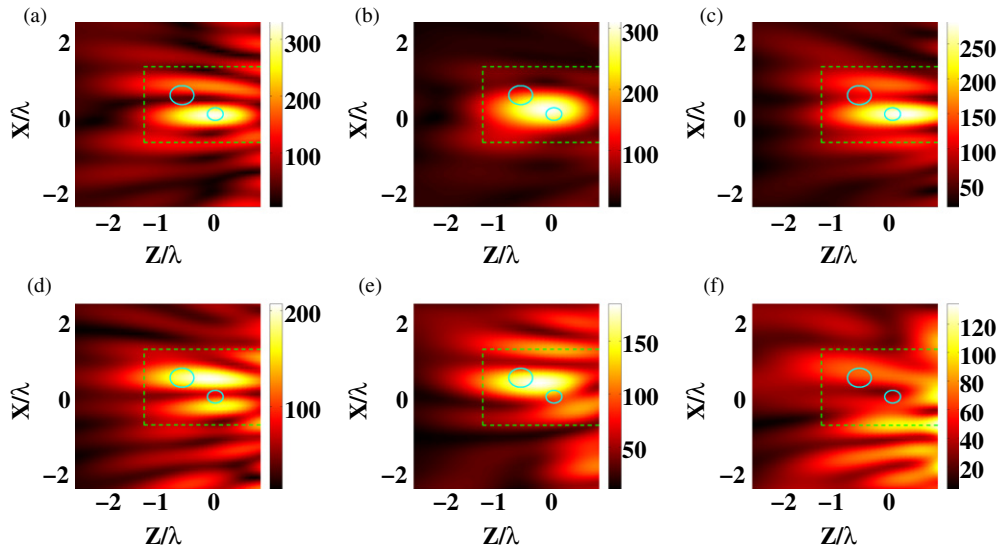


Figure 10. Intensity in the (x, z) plane at $y = 0$ of the electric field given by the six eigenvectors corresponding to the six highest eigenvalues. The structural noise, $\text{Err}_s = 682\%$ and $\text{Err}_d = 2\%$, is obtained with $l_c = \lambda/10$ and $\sigma(\varepsilon_f) = 0.125\varepsilon_b$. Top: the intensity corresponding to the first, second and third eigenvalues. Bottom: the intensity corresponding to the fourth, fifth and sixth eigenvalues.

5.3.2. Influence of the correlation length. In this section, we analyse the influence of the clutter correlation length on the reconstruction. We first consider clutters with standard variations $\sigma(\varepsilon_f) \approx 0.06\varepsilon_b$ and noise levels $\text{Err}_s \approx 200\%$, that are similar to the one taken for figure 4 and increase the correlation lengths l_c from $\lambda/10$ to λ . At this moderate noise level, we observe that the DORT focusing properties weakly depend on the correlation lengths. Whatever the correlation lengths, the six dominant eigenvectors yield incident fields that focus on each scatterer. The inversion-DORT reconstructions are quite accurate and resemble that obtained for the uncorrelated clutter, figure 4.

In contrast, at higher standard deviations, $\sigma(\varepsilon_f) \approx 0.1\varepsilon_b$ and higher noise levels $\text{Err}_s \approx 400\%$, the DORT focusing properties depend strongly on the correlation lengths. At $l_c = \lambda/10$, one obtains three eigenvectors focusing on each target and the reconstructions are good and similar to that displayed in figure 9.

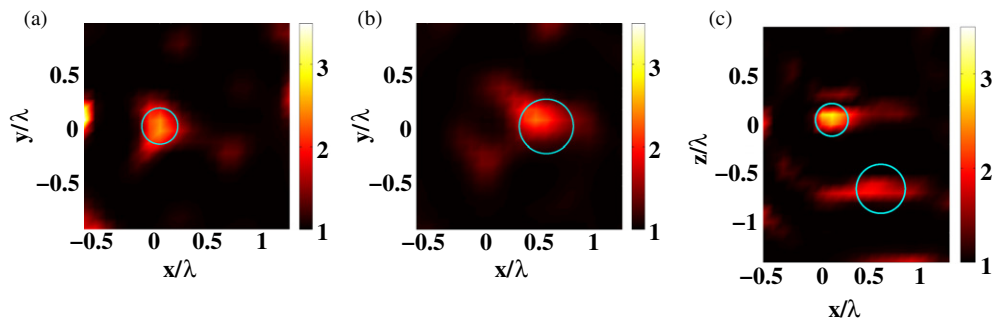


Figure 11. The same as figure 4 but the clutter is defined by $l_c = \lambda/10$, $\sigma(\varepsilon_f) = 0.125\varepsilon_b$ yielding $\text{Err}_s = 682\%$ and $\text{Err}_d = 2\%$.

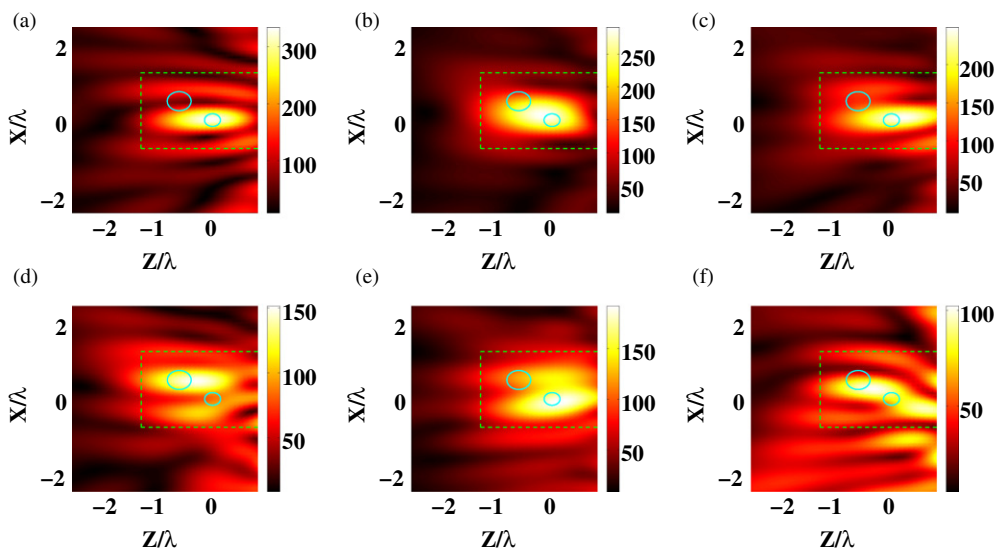


Figure 12. The same as figure 10, but the clutter with the correlation length $l_c = \lambda/2$, $\sigma(\varepsilon_f) = 0.1\varepsilon_b$, where the clutter environment corresponds to 400% noise.

For $l_c = \lambda/2$, it becomes difficult to localize the deepest scatterer with the first six dominant eigenvector intensity maps, as seen in figure 12. However, the inversion-DORT method permits to retrieve accurately both targets, figure 13.

When $l_c = \lambda$, the focusing properties of the DORT fields are further deteriorated. Moreover, the eigenvectors that are roughly focusing on the least echogeneous target do not correspond to the third, fourth and sixth highest eigenvalues. In this case, a careful study of the intensity maps of the eigenvectors in order to determine the most significant eigenvectors is required. This analysis implies that we have some *a priori* information on the sought targets. With this additional procedure, the inversion-DORT reconstruction obtained with the six most significant eigenvectors yields a good estimate of the targets. Note that, similarly to the $l_c = \lambda/2$ case, the localization of the targets given by inversion-DORT is much better than that obtained with DORT alone.

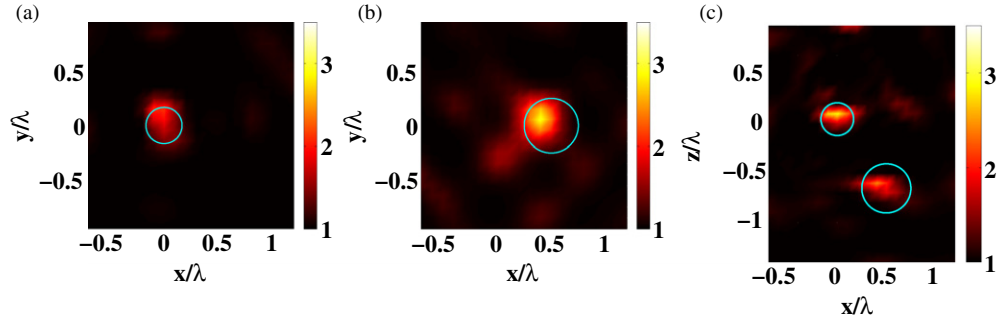


Figure 13. The same as figure 4, except that the clutter environment corresponds to 400% noise, with the correlation length $l_c = \lambda/2$, $\sigma(\varepsilon_f) = 0.1\varepsilon_b$.

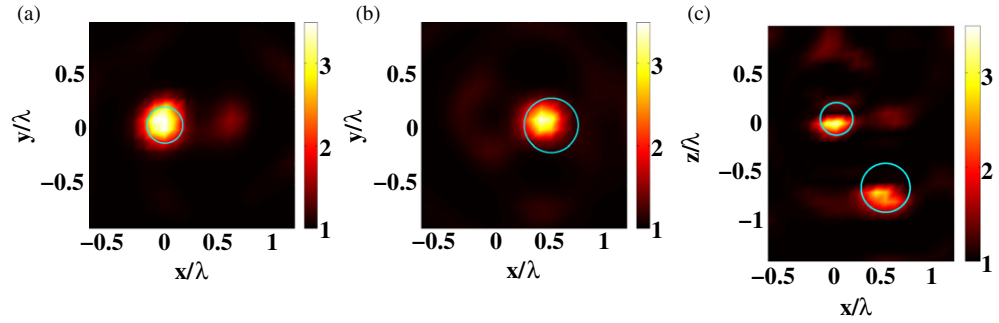


Figure 14. The same as figure 4, the clutter is defined by $l_c = \lambda/10$, $\sigma(\varepsilon_f) = 0.055\varepsilon_b$ but one has chosen a specific realization where $\text{Err}_s = 182\%$ and $\text{Err}_d = 54\%$, implying a significant coupling between the spheres and the clutter.

5.3.3. Influence of the coupling between the targets and the clutter. Up to now, we have considered configurations in which the targets and the clutter are weakly coupled, $\text{Err}_d < 5\%$. In other terms, the field detected by the antennas can be modelled by the coherent sum of the field radiated by the spheres in the homogeneous background medium with the field radiated by the clutter alone. In this section, we investigate the performance of the inversion-DORT algorithm when there is multiple scattering between the targets and the clutter. We chose a configuration with the same statistical parameters as that taken in figure 4 but used a specific clutter realization that yielded $\text{Err}_d = 54\%$, $\text{Err}_{\text{born}} = 123\%$ while $\text{Err}_s = 182\%$. The coupling between the targets and the clutter is caused by the presence of highly contrasted inhomogeneities close to the targets. The inversion-DORT reconstruction displayed in figure 14 shows that this configuration can be handled without difficulty with our algorithm.

To summarize this part, we have shown that the inversion-DORT algorithm provides satisfactory images of the targets even when they are buried in clutters with high standard deviations (up to $0.125\varepsilon_b$) or large correlation lengths in which the focusing properties of the DORT fields are deteriorated. In the following section, we stress the importance of using a nonlinear inversion scheme and the full polarized data to obtain this performance.

5.4. Interest of using a nonlinear inversion scheme and full polarized data

The hybrid inversion-DORT method used in this work is based on a nonlinear inversion scheme. In other terms, both the permittivity and the total field inside the investigating domain Ω are

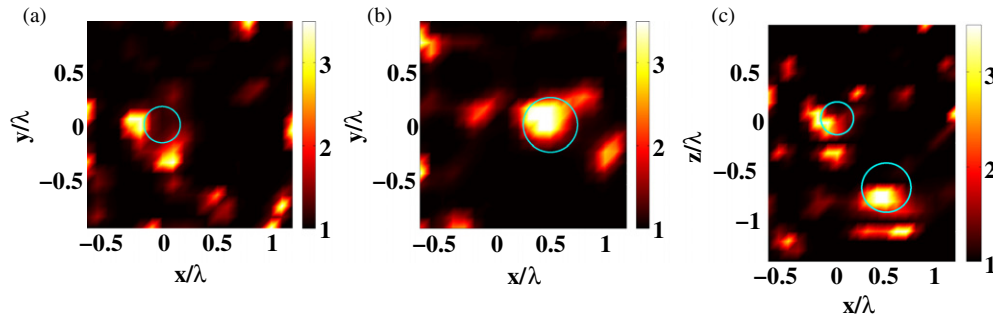


Figure 15. The same as figure 4 but a linear-inversion-DORT procedure assuming single scattering is used for getting the reconstructions.

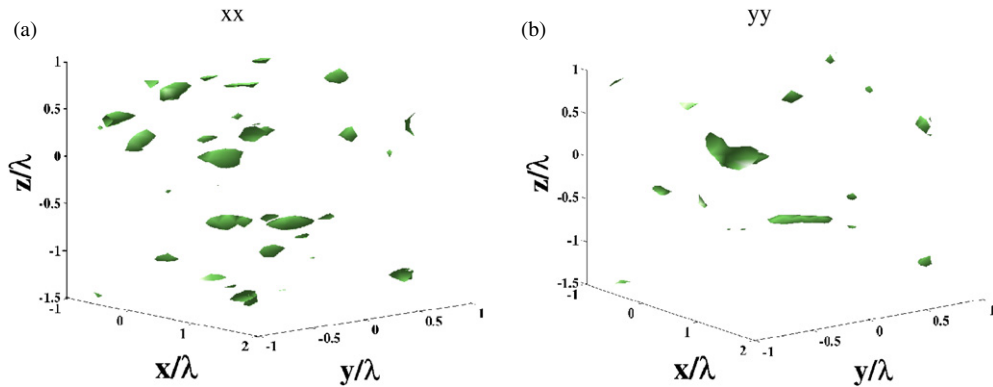


Figure 16. Iso-surface of the reconstructed permittivity profile at $\varepsilon = 2$ using the inversion-DORT procedure for the same configuration as that used in figure 5. (a) The antennas are oriented along the x direction and the scattered field is detected along the x direction only. (b) The antennas are oriented along the y direction and the scattered field is detected along the y direction only.

unknown and sought by the algorithm. In this section, we consider a simpler linear-inversion-DORT technique in which the total field inside Ω is assumed to be the incident field (Born approximation). The linear-inversion-DORT scheme is implemented easily from the inversion-DORT algorithm by putting the search directions for the total field to zero and setting the total field equal to the incident field. The interest of the linear-inversion technique is that it is much faster than the nonlinear-inversion version. Unfortunately, it is seen in figure 15 that the linear-inversion-DORT scheme fails to retrieve the targets even in the least noisy configuration, $\text{Err}_s = 174\%$, corresponding to figure 4. In this configuration, the coupling between the targets and the clutter is weak but there is some multiple scattering within the clutter and within the targets as indicated by $\text{Err}_{\text{born}} = 48\%$. The latter is sufficient to deteriorate significantly the performances of the linear-inversion scheme. This example stresses the importance of using nonlinear-inversion techniques even for moderately contrasted clutter $\sigma(\varepsilon_f) \approx 0.06\varepsilon_b$ and even if there is no coupling between the targets and the clutter, $\text{Err}_d < 5\%$.

Another reason for the performance of our imaging scheme in highly noisy environment is that we use the three orientations of the antennas for illuminating and observing the scene. We are thus able to generate several DORT fields focusing on each target. We now consider a simpler imaging configuration where the emitting and receiving antennas are oriented only along the x - or y -axis so that only scalar data are collected as in an acoustical problem. In this case, only one DORT field focusing on each target can be found. In figure 16, we plot

the reconstructions obtained with these truncated data for the same geometry as that used in figure 5. We observe a significant deterioration of the results as compared to figure 5(a), the reconstruction error on the contrast reaching $\text{Err}_\chi = 191\%$ and $\text{Err}_\chi = 177\%$ for the x and y orientations, to be compared to $\text{Err}_\chi = 62\%$ for the full polarized data. Hence, even for the least noisy experiment ($\text{Err}_s = 171\%$), the use of the full polarized data appears to ameliorate significantly the reconstruction.

6. Conclusion

In conclusion, we have numerically studied the imaging issue of targets buried in a random inhomogeneous medium with monochromatic data. We have shown that using the three-dimensional vectorial time reversal operator (DORT method), one can generate different incident fields that focus selectively on each target. We have proposed a hybrid method, named inversion-DORT, that uses the answer of the medium to these DORT fields for reconstructing the permittivity of a region of interest with a nonlinear optimization scheme. The inversion-DORT procedure localizes better the targets than the DORT procedure alone, especially in the z direction, and is more efficient than a classical inversion scheme for characterizing the targets, with significantly less computational burden. It permits us to handle very noisy configurations, with clutter standard deviation up to 12%, that support multiple scattering. Lastly, we have stressed the importance of using nonlinear inversion algorithms and full polarized data for achieving this performance. A promising extension of this work will be to use full time-domain data in order to consider targets that are buried further away from the antennas [16, 39] or supporting stronger multiple scattering [15], and to consider more complex configurations (targets buried in a half inhomogeneous medium or placed above a substrate). Finally, we would like to stress that the combined DORT and inversion procedure can be useful in imaging applications where there is no structural noise (such as optical imaging of manufactured nanostructures), because it permits us to reduce drastically the computation time and memory burden.

References

- [1] Ammari H, Garnier J and Solna K 2012 A statistical approach to target detection and localization in the presence of noise *Waves Random Complex Media* **22** 40–65
- [2] Reid D B 1979 An algorithm for tracking multiple targets *IEEE Trans. Autom. Control* **24** 843–54
- [3] Liu D, Kang G, Li L, Chen Y, Vasudevan S, Joines W, Liu Q H, Krolik J and Carin L 2005 Electromagnetic time-reversal imaging of a target in a cluttered environment *IEEE Trans. Antennas Propag.* **53** 3058–66
- [4] Fouda A E and Teixeira F L 2012 Imaging and tracking of targets in clutter using differential time-reversal techniques *Waves Random Complex Media* **22** 66–108
- [5] Prada C and Fink M 1994 Eigenmodes of the time reversal operator: a solution to selective focusing in multiple-target media *Wave Motion* **20** 151–63
- [6] Prada C, Manneville S, Spoliansky D and Fink M 1996 Decomposition of the time reversal operator: detection and selective focusing on two scatterers *J. Acoust. Soc. Am.* **9** 2067–76
- [7] Tortel H, Micolau G and Saillard M 1999 Decomposition of the time reversal operator for electromagnetic scattering *J. Electromagn. Waves Appl.* **13** 687–719
- [8] Micolau G and Saillard M 2003 DORT method as applied to electromagnetic sensing of buried objects *Radio Sci.* **38** 1038
- [9] Moss C D, Teixeira F L, Yang Y E and Kong J A 2002 Finite-difference time-domain simulation of scattering from objects in continuous random media *IEEE Trans. Geosci. Remote Sens.* **40** 178–86
- [10] Moss C D, Teixeira F L and Kong J A 2002 Detection of targets in continuous random media: a numerical study using the angular correlation function *Microw. Opt. Technol. Lett.* **33** 242–7
- [11] Cmielewski O, Saillard M, Belkebir K and Tortel H 2006 On the characterization of buried targets under a rough surface using the Wigner–Ville transformation *IEEE Geosci. Remote Sens. Lett.* **3** 442–6

- [12] Borcea L, Papanicolaou G, Tsogka C and Berryman J 2002 Imaging and time reversal in random media *Inverse Problems* **18** 1247–79
- [13] Cheney M 2001 The linear sampling method and the MUSIC algorithm *Inverse Problems* **17** 591–5
- [14] Yavuz M E and Teixeira F L 2006 Full time-domain DORT for ultrawideband electromagnetic fields in dispersive, random inhomogeneous media *IEEE Trans. Antennas Propag.* **54** 2305–15
- [15] Yavuz M E and Teixeira F L 2008 Space-frequency ultrawideband time-reversal imaging *IEEE Trans. Geosci. Remote Sens.* **46** 1115–24
- [16] Borcea L, Papanicolaou G and Tsogka C 2006 Adaptive interferometric imaging in clutter and optimal illumination *Inverse Problems* **22** 1405–36
- [17] Belkebir K, Chaumet P C and Sentenac A 2006 Influence of multiple scattering on three-dimensional imaging with optical diffraction tomography *J. Opt. Soc. Am. A* **23** 586–95
- [18] Litman A and Crocco L 2009 Testing inversion algorithms against experimental data: 3D targets *Inverse Problems* **25** 020201
- [19] Semenov S Y, Bulyshev A E, Abubakar A, Posukh V G, Sizov Y E, Souvorov A E, van den Berg P M and Williams T C 2005 Microwave-tomographic imaging of the high dielectric-contrast objects using different image-reconstruction approaches *IEEE Trans. Microw. Theory Tech.* **53** 2284–94
- [20] Maire G, Girard J, Drsek F, Giovannini H, Talneau A, Belkebir K, Chaumet P C and Sentenac A 2010 Experimental inversion of optical diffraction tomography data with a nonlinear algorithm in the multiple scattering regime *J. Mod. Opt.* **57** 746–55
- [21] Girard J, Maire G, Giovannini H, Talneau A, Belkebir K, Chaumet P C and Sentenac A 2010 Nanometric resolution using far-field optical tomographic microscopy in the multiple scattering regime *Phys. Rev. A* **82** 061801
- [22] Ruan Y *et al* 2012 Tomographic diffractive microscopy with a wavefront sensor *Opt. Lett.* **37** 1631–3
- [23] Purcell E M and Pennypacker C R 1973 Scattering and absorption of light by nonspherical dielectric grains *Astrophys. J.* **186** 705–14
- [24] Chaumet P C, Sentenac A and Rahmani A 2004 Coupled dipole method for scatterers with large permittivity *Phys. Rev. E* **70** 036606
- [25] Jackson J D 1975 *Classical Electrodynamics* 2nd edn (New York: Wiley)
- [26] Chambers D H and Berryman J G 2004 Analysis of the time-reversal operator for a small spherical scatterer in an electromagnetic field *IEEE Trans. Antennas Propag.* **52** 1729–38
- [27] Roger A 1981 Newton–Kantorovitch algorithm applied to an electromagnetic inverse problem *IEEE Trans. Antennas Propag.* **29** 232–8
- [28] Chew W C and Wang Y M 1990 Reconstruction of two-dimensional permittivity distribution using distorted Born iterative method *IEEE Trans. Med. Imaging* **9** 218–25
- [29] Chen F C and Chew W C 1998 Experimental verification of super resolution in nonlinear inverse scattering *Appl. Phys. Lett.* **72** 3080–2
- [30] Kleinman R E and van den Berg P M 1992 A modified gradient method for two-dimensional problems in tomography *J. Comput. Appl. Math.* **42** 17–35
- [31] Souriau L, Duchêne B, Lesselier D and Kleinman R E 1996 Modified gradient approach to inverse scattering for binary objects in stratified media *Inverse Problems* **12** 463–81
- [32] van den Berg P M and Kleinman R E 1997 A contrast source inversion method *Inverse Problems* **13** 1607–20
- [33] Abubakar A, van den Berg P M and Kooij B J 2000 A conjugate gradient contrast source technique for 3D profile inversion *IEICE Trans. Electron. E* **83-C** 1864–74
- [34] Abubakar A and van den Berg P M 2002 The contrast source inversion method for location and shape reconstructions *Inverse Problems* **18** 495–510
- [35] Belkebir K and Tijhuis A G 2001 Modified² gradient method and modified Born method for solving a two-dimensional inverse scattering problem *Inverse Problems* **17** 1671–88
- [36] Dubois A, Belkebir K and Saillard M 2004 Localization and characterization of two-dimensional targets buried in a cluttered environment *Inverse Problems* **20** S63–79
- [37] Press W H, Teukolski S A, Vetterling W T and Flannery B P 1986 *Numerical Recipes. The Art of Scientific Computing* (Cambridge: Cambridge University Press)
- [38] Belkebir K, Bonnard S, Pezin F, Sabouroux P and Saillard M 2000 Validation of 2D inverse scattering algorithms from multi-frequency experimental data *J. Electromagn. Waves Appl.* **14** 1637–67
- [39] Dubois A, Belkebir K, Catapano I and Saillard M 2009 Iterative solution of the electromagnetic inverse scattering problem from the transient scattered field *Radio Sci.* **44** 14